Dynamic Analysis of MMC-Based MTDC Grids : Use of MMC Energy to Improve Voltage Behavior

Julian Freytes, Samy Akkari, Pierre Rault, Mohamed Moez Belhaouane, François Gruson, Frédéric Colas, Xavier Guillaud

Dynamic Analysis of MMC-Based MTDC Grids: Use of MMC Energy to Improve Voltage Behavior

Julian Freytes, *Member, IEEE*, Samy Akkari, Pierre Rault, Mohamed Moez Belhaouane, François Gruson, Frédéric Colas and Xavier Guillaud, *Member, IEEE*

***Abstract*—This article deals with DC voltage dynamics of Multi-Terminal HVDC grids (MTDC) with energy-based controlled Modular Multilevel Converters (MMC) adopting the commonly used power-voltage droop control technique for power flow dispatch. Special focus is given on the energy management strategies of the MMCs and their ability to influence on the DC voltage dynamics. First, it is shown that decoupling the MMC energy from the DC side, causes large and undesired DC voltage transient after a sudden power flow change. This occurs when this energy is controlled to a fixed value regardless of the DC voltage level. Second, the Virtual Capacitor Control technique is implemented in order to improve the results. However, its limitations on droop-based MTDC grids are highlighted. Finally, a novel energy management approach is proposed to improve the performance of the later method. These studies are performed with detailed MMC models suitable for the use of linear analysis techniques. The derived MTDC models are validated against time-domain simulations using detailed EMT MMC models with 400 sub-modules per arm.**

***Index Terms*—Multi-Terminal HVDC Transmission, Modular Multilevel Converter, State-Space Modeling, Singular Value Decomposition, Energy controllers, Droop control**

I. Introduction

THE Modular Multilevel Converter is the state-of-the-art of High-Voltage DC transmission systems (HVDC) [1], and it's suitable for Multi-Terminal DC grids [2].

The dynamic analysis of power-voltage droop controlled MTDC grids was widely studied considering *2-level* Voltage Source Converters (VSC) [3]–[7]. As discussed in [4], the main parameters that govern the DC dynamics are the droop gains and the total stored energy in the DC grid. When considering *2-level* VSCs, the stored energy in the DC grid is determined by the DC bus capacitors of converters, so the droop gain is the only parameter that can be modified to have a direct impact on the DC-side dynamics. However, with a single tunable gain, the options for improving the dynamics are rather limited. In consequence, some improvements were already proposed, as in [5], where lead-lag compensators are added to the controller structure. In [6], the DC voltage droop control structure is redefined for dealing directly with the energy of the grid, with promising results. In [7] and [8], specific controllers are proposed to damp DC resonances. Even though some of these papers mention the MMC, the converters are modeled or controlled similarly as *2-level* VSCs (as e.g. [8]). However, the way that the internal energy of the MMC is managed may influence directly the dynamics of the system. In [9], the possibility of using the internally stored energy in the MMCs for supporting the AC grid frequency is studied. This energy may also be used to support the DC grid [10].

Indeed, depending on the adopted MMC control strategy, the internal energy may be largely decoupled from the DC voltage [11]. In [12], the impact of the MMC control algorithm on the droop-controlled MTDC has been analyzed with time domain simulations. It concludes that the decoupling capability of the MMC internally stored energy has a considerable impact on the dynamics of the MTDC grids: a part of the total energy stored in the DC grid relies on the MMC controller structure. In [13], similar conclusions were obtained regarding MMC-based point-to-point HVDC links and, for this reason, a modification on the MMC energy controllers was introduced. Moreover, [14] shows that it is possible to virtually enhance the DC energy by using the virtual capacitor concept.

Until now, the effect of the MMC control on the MTDC dynamics has been only analyzed through time-domain simulations or using simplified MMC models. In order to quantify the impact of MMC energy controllers on the DC grid dynamics, a Linear Time Invariant (LTI) modeling approach is of great interest for these studies. To do so, a suitable dynamic model of the MMC is needed. In the literature, dynamic phasors domain [15] or multiple dq frames [16] has been proposed as a modeling approach for developing an LTI model. This paper is based on [17], where a full dynamic non-linear MMC model with Steady-State Time Invariant solution (SSTI) was developed and further linearized and studied in [18], where the control strategy of the converter can be easily modified.

While articles [15]–[18] consider a dynamic analysis of a single MMC with a simplified environment (AC and DC sources), this paper considers an MTDC grid modeled with detailed MMC representations. Based on this modeling, an

Manuscript received December 26, 2017; revised March 2, 2018; accepted August 25, 2018. Date of publication, September xx, 2018; date of current version, September xx, 2018. Paper no. TPWRD-01563-2017. *(Corresponding author: Julian Freytes).*

J. Freytes was with Centrale Lille, Lille 59651, France, when this work was conducted, and is now with Grid solutions, GE Power, Massy 91300, France (e-mail: julian.freytes@ge.com).

M. M. Belhaouane and X. Guillaud are with the Laboratoire d'Electrotechnique et d'Electronique de Puissance of Lille (L2EP), Centrale Lille, Lille 59651, France (e-mail: mohamed-moez.belhaouane@centralelille.fr; xavier.guillaud@centralelille.fr).

F. Gruson and F. Colas are with the Laboratoire d'Electrotechnique et d'Electronique de Puissance of Lille (L2EP), Arts et Metiers ParisTech, Lille 59046, France (e-mail: francois.gruson@ensam.eu; frederic.colas@ensam.eu).

S. Akkari and P. Rault are with the Réseau de Transport d'Électricité (RTE), Paris 92919, France (e-mail: pierre.rault@rte-france.com; samy.akkari@rte-france.com).

Color versions of one or more of the figures in this paper are available online at http://ieeexplore.ieee.org,

Digital Object Identifier xx.xxx

in depth dynamic analysis is provided and different types of MMC controllers are evaluated and precisely compared, hence highlighting the influence of the energy management of the MMC on the system dynamics.

The main contributions of this paper are twofold:

- Detailed LTI modeling of MMC-based MTDC grid based on accurate MMC models which allow to take into account different controllers. Frequency dependent cable models are used to represent the DC grid dynamics. The obtained model is compared against an Electro-Magnetic Transient simulation (EMT) with switching models for the MMCs.
- Comparison of three MMC Energy Management Control strategies: the first one considers a constant energy reference as in [18]; the second one considers the method from [14]; and the third one is a novel strategy based on the derivative of the DC voltage. The main characteristics of each one are highlighted throughout the paper.

The rest of the paper is organized as follows. In Section II, a LTI model of a droop-controlled single terminal MMC in double Synchronous Rotating Reference Frame (SRRF) considering AC and DC sides is developed as a fundamental block. Then, in Section III, a linear MTDC grid is created with the concatenation of the aforementioned blocks, where each MMC is controlled with an energy-based strategy with constant energy reference. The dynamic performance of the MTDC grid is evaluated using the Singular Value Decomposition method (SVD). In Section IV, different energy management control variants are assessed based on the dynamic analysis of the resultant MTDC grid.

II. MMC Modeling and Control for Coupling with MTDC System

In this section, a full SSTI MMC model including an *Energy-based* controller is developed based on [17] and [18]. The nomenclature used in this paper is defined in [18].

A. Continuous MMC Arm Averaged Model

1) Model with "Upper-Lower" representation in abc frame: The Arm Averaged Model (AAM) of the MMC is recalled in Fig. 1 [19]. The model presents, for each phase, a leg consisting of an upper and a lower arm. Each arm includes an inductance L_{arm}, an equivalent resistance R_{arm} and an aggregated capacitance $C_{arm} = C/N$, where N is the number of submodules per-arm and C is the capacitor of each SM.

The arm currents $[\boldsymbol{i^U_{abc}}, \boldsymbol{i^L_{abc}}]$ are a combination of a DC part, an alternating component at ω and potentially an additional term at 2ω (the same stands for the modulated voltages $[\boldsymbol{v^U_{mabc}}, \boldsymbol{v^L_{mabc}}]$ and the modulation indices $[\boldsymbol{m^U_{abc}}, \boldsymbol{m^L_{abc}}]$). Since the arm capacitors $[\boldsymbol{v^U_{Cabc}}, \boldsymbol{v^L_{Cabc}}]$ are being charged and discharged by the modulated currents obtained by the multiplication of their respective arm currents and modulation indices (each with DC, ω and 2ω), the voltages include a DC, ω and 2ω but also 3ω and 4ω components (this last part is negligible as shown in [20]). This multiple frequency content in the "Upper" and "Lower" variables inhibit the application of a single Park transformation to the system equations to develop a full dqz model suitable for linearization. Nevertheless, it is possible to isolate the main frequency content of the variables transforming them as described in the following.

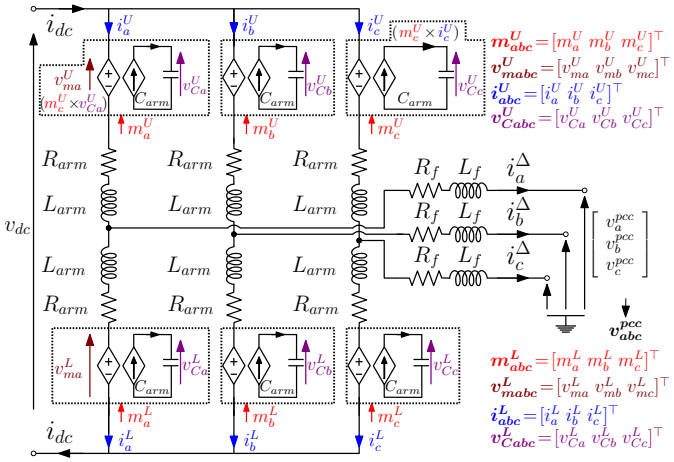

Fig. 1. MMC Arm Averaged Model with "Upper-Lower" representation.

Table I
MMC variables in Σ-Δ representation in *abc* frame

Variables with ω and 3ω	Variables with DC and -2ω
$\boldsymbol{i^\Delta_{abc}} \stackrel{\text{def}}{=} \boldsymbol{i^U_{abc}} - \boldsymbol{i^L_{abc}}$	$\boldsymbol{i^\Sigma_{abc}} \stackrel{\text{def}}{=} (\boldsymbol{i^U_{abc}} + \boldsymbol{i^L_{abc}})/2$
$\boldsymbol{v^\Delta_{mabc}} \stackrel{\text{def}}{=} (-\boldsymbol{v^U_{mabc}} + \boldsymbol{v^L_{mabc}})/2$	$\boldsymbol{v^\Sigma_{mabc}} \stackrel{\text{def}}{=} (\boldsymbol{v^U_{mabc}} + \boldsymbol{v^L_{mabc}})/2$
$\boldsymbol{v^\Delta_{Cabc}} \stackrel{\text{def}}{=} (\boldsymbol{v^U_{Cabc}} - \boldsymbol{v^L_{Cabc}})/2$	$\boldsymbol{v^\Sigma_{Cabc}} \stackrel{\text{def}}{=} (\boldsymbol{v^U_{Cabc}} + \boldsymbol{v^L_{Cabc}})/2$
$\boldsymbol{m^\Delta_{abc}} \stackrel{\text{def}}{=} \boldsymbol{m^U_{abc}} - \boldsymbol{m^L_{abc}}$	$\boldsymbol{m^\Sigma_{abc}} \stackrel{\text{def}}{=} \boldsymbol{m^U_{abc}} + \boldsymbol{m^L_{abc}}$

2) Modeling with "Σ-Δ" representation in abc frame: For deriving the dynamics of the AAM, all the MMC variables are transformed from the "Upper-Lower" representation to "Σ-Δ", as summarized in Table I (bold variables represent vectors). In steady state, "Δ" variables are sinusoidal at the fundamental grid frequency ω, while "Σ" variables contain a sinusoidal oscillation at -2ω superimposed to a DC-component [17].

3) Model with "Σ-Δ" representation in dqz frame: Once the main frequencies are identified, Park transformation at -2ω is applied to the "Σ" variables, obtaining the common-mode currents $\boldsymbol{i^\Sigma_{dqz}} = [i^\Sigma_d, i^\Sigma_q, i^\Sigma_z]^\top$, the common-mode modulated voltages $\boldsymbol{v^\Sigma_{mdqz}} = [v^\Sigma_{md}, v^\Sigma_{mq}, v^\Sigma_{mz}]^\top$, modulation indices sum $\boldsymbol{m^\Sigma_{dqz}} = [m^\Sigma_d, m^\Sigma_q, m^\Sigma_z]^\top$ and the arm capacitors $\boldsymbol{v^\Sigma_{Cdqz}} = [v^\Sigma_{Cd}, v^\Sigma_{Cq}, v^\Sigma_{Cz}]^\top$. Furthermore, Park transformation at ω is applied to the "Δ" variables, resulting in the grid currents $\boldsymbol{i^\Delta_{dq}} = [i^\Delta_d, i^\Delta_q]^\top$, the modulated voltages $\boldsymbol{v^\Delta_{mdq}} = [v^\Delta_{md}, v^\Delta_{mq}]^\top$, modulation indices $\boldsymbol{m^\Delta_{dq}} = [m^\Delta_d, m^\Delta_q]^\top$ and arm capacitor voltages difference $\boldsymbol{v^\Delta_{Cdq}} = [v^\Delta_{Cd}, v^\Delta_{Cq}]^\top$. The zero-sequence v^Δ_{Cz} oscillates at 3ω, so an auxiliary virtual variable is also used to be able to represent the magnitude and phase of the oscillating component, i.e. $\boldsymbol{v^\Delta_{CZ}} = [v^\Delta_{CZ_d}, v^\Delta_{CZ_q}]^\top$. In this way, the result is $\boldsymbol{v^\Delta_{CdqZ}} = [(\boldsymbol{v^\Delta_{Cdq}})^\top, (\boldsymbol{v^\Delta_{CZ}})^\top]^\top$. These transformations allow to obtain a MMC model in SRRF with Steady-State Time Invariant solution (SSTI) suitable for linearization and further analysis. The main equations of the MMC model in dqz are given in the Appendix B, and the complete mathematical development can be found in [17].

The MMC stored energy W^Σ_z is calculated from the dqz

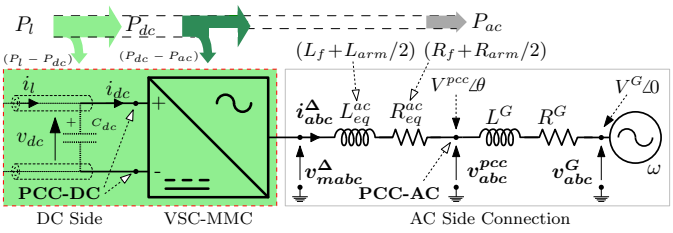

Fig. 2. MMC Connected to AC and DC equivalent grids.

components as in (1a), where $C_{mmc} = 6 \times C_{arm}$. However, it can be approximated as proportional only to $(v_{Cz}^{\Sigma})^2$ for analysis purposes as shown in (1b), since it corresponds to the sum of all the MMC capacitor voltages [21]. The complete calculation is shown in Appendix C.

$$W_z^{\Sigma} = \frac{1}{2} C_{mmc} \left(v_{Cz}^{\Sigma}\right)^2 + \frac{C_{mmc}}{4} \left[\left(v_{Cd}^{\Sigma}\right)^2 + \left(v_{Cq}^{\Sigma}\right)^2 \right] \quad (1a)$$
$$+ \frac{C_{mmc}}{4} \left[\left(v_{Cd}^{\Delta}\right)^2 + \left(v_{Cq}^{\Delta}\right)^2 + \left(v_{CZ_d}^{\Delta}\right)^2 + \left(v_{CZ_q}^{\Delta}\right)^2 \right]$$
$$W_z^{\Sigma} \approx \frac{1}{2} C_{mmc} \left(v_{Cz}^{\Sigma}\right)^2 \quad (1b)$$

B. MMC model in SRRF interfacing AC and DC grids

In Fig. 2, the single terminal MMC model with its AC and DC sides Points of Common-Coupling is shown (PCC-AC and PCC-DC, respectively). The variables $P_l = v_{dc} i_l$ and $P_{dc} = v_{dc} i_{dc}$ are powers interacting on the PCC-DC, while P_{ac} correspond to the output power on the PCC-AC.

1) DC-side connection: At this stage, the DC bus is modeled by (2), where C_{dc} represents the sum of all the equivalent capacitance of the cables connected to the PCC-DC and i_l is the equivalent current from the DC grid.

$$C_{dc} \frac{dv_{dc}}{dt} = i_l - i_{dc} = i_l - 3i_z^{\Sigma} \quad (2)$$

2) AC-side connection: The AC current dynamics $\boldsymbol{i_{dq}^{\Delta}}$ are modeled as:

$$L \frac{d\boldsymbol{i_{dq}^{\Delta}}}{dt} = \boldsymbol{v_{mdq}^{\Delta}} - \boldsymbol{v_{dq}^{G}} - R\boldsymbol{i_{dq}^{\Delta}} - \omega L \begin{bmatrix} +i_q^{\Delta} \\ -i_d^{\Delta} \end{bmatrix} \quad (3)$$

where $L \stackrel{\text{def}}{=} L_{eq}^{ac} + L^G$, $R \stackrel{\text{def}}{=} R_{eq}^{ac} + R^G$ and $\boldsymbol{v_{dq}^{G}} = [v_d^G, v_q^G]^\top$. The voltages $\boldsymbol{v_{dq}^{pcc}} = [v_d^{pcc}, v_q^{pcc}]^\top$ are calculated as follows [22]:

$$\boldsymbol{v_{dq}^{pcc}} = \frac{L_{eq}^{ac}}{L} \boldsymbol{v_{dq}^{G}} + \left(\frac{R^G L_{eq}^{ac} - R_{eq}^{ac} L^G}{L} \right) \boldsymbol{i_{dq}^{\Delta}} + \frac{L^G}{L} \boldsymbol{v_{mdq}^{\Delta}} \quad (4)$$

An overview of the model structure corresponding to the MMC altogether with the AC and DC side equations is shown in Fig. 3. The dynamic equations of $\boldsymbol{v_{mdq}^{\Delta}}$, $\boldsymbol{v_{mdqz}^{\Sigma}}$, $\boldsymbol{v_{Cdqz}^{\Sigma}}$, $\boldsymbol{v_{CdqZ}^{\Delta}}$, and $\boldsymbol{i_{dqz}^{\Sigma}}$ can be found in the Appendix B.

C. MMC Energy-based control

Based on the proposed SSTI MMC model, a suitable controller in dq frame can be designed. In this sub-section, the *Energy-based* controller from [18] is recalled (variables with superscript "*" correspond to reference values). However, the dq frame from the control is not the same as for the MMC.

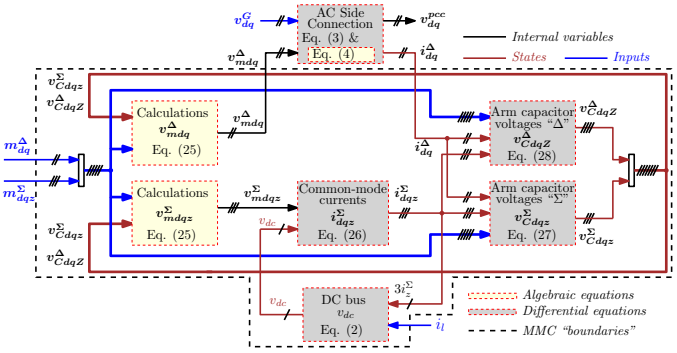

Fig. 3. MMC model with Steady-State Time-Invariant solution.

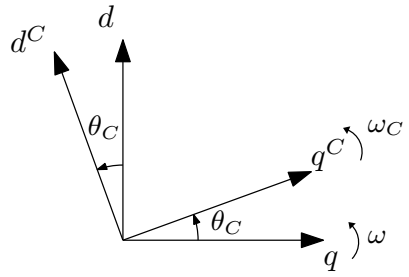

(a) SRRFs $\boldsymbol{dq} = [d\ q]^\top$ and $\boldsymbol{dq^C} = [d^C\ q^C]^\top$.

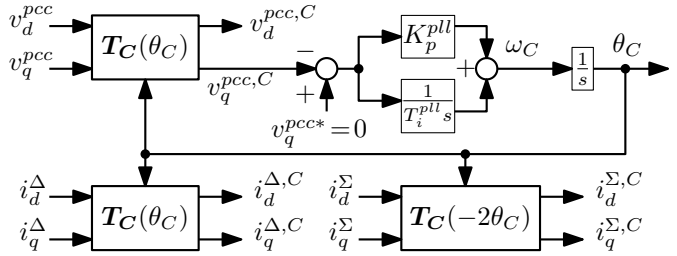

(b) PLL structure and measures.

Fig. 4. Simplified Phase Locked Loop for SSTI-MMC control.

1) Phase-Locked Loop: Indeed, the dq variables from the AC side of the MMC (currents $\boldsymbol{i_{dq}^{\Delta}}$ and voltages $\boldsymbol{v_{dq}^{pcc}}$) are referred to the SRRF at the frequency ω from the AC grid (i.e. axes $\boldsymbol{dq}$ in Fig. 4(a)). The angular frequency ω is estimated by a Phase-Locked Loop (PLL) at the PCC-AC, obtaining ω_C as well as the estimation of the angle θ between the phasors V^G and V^{pcc} given by θ_C. In the following, the variables $\boldsymbol{v_{dq}^{pcc}}$ and $\boldsymbol{i_{dq}^{\Delta}}$, are linked to the frame dq^C with the transformation $\boldsymbol{T_C}(\theta_C)$ as shown in (5) for a generic variable $\boldsymbol{x_{dq}} = [x_d, x_q]^\top$, obtaining $\boldsymbol{x_{dq}^C} = [x_q^C, x_q^C]^\top$ [23]. The inverse $\boldsymbol{T_C^{-1}}$ is also used in order to calculate the physical output voltages, as it is described in the following sub-section.

$$\underbrace{\begin{bmatrix} x_d^C \\ x_q^C \end{bmatrix}}_{\substack{\text{Measured signals} \\ \text{sent to controller}}} = \underbrace{\begin{bmatrix} +\cos(\theta_C) & -\sin(\theta_C) \\ +\sin(\theta_C) & +\cos(\theta_C) \end{bmatrix}}_{\boldsymbol{T_C}(\theta_C)} \underbrace{\begin{bmatrix} x_d \\ x_q \end{bmatrix}}_{\substack{\text{Physical} \\ \text{variables}}} \quad (5)$$

The structure of the PLL is shown in Fig. 4(b), where the transformations $\boldsymbol{T_C}(\theta_C)$ applied to $\boldsymbol{v_{dq}^{pcc}}$, $\boldsymbol{i_{dq}^{\Delta}}$ and also to the MMC circulating currents $\boldsymbol{i_{dq}^{\Sigma}}$ with $\boldsymbol{T_C}(-2\theta_C)$ can be observed.

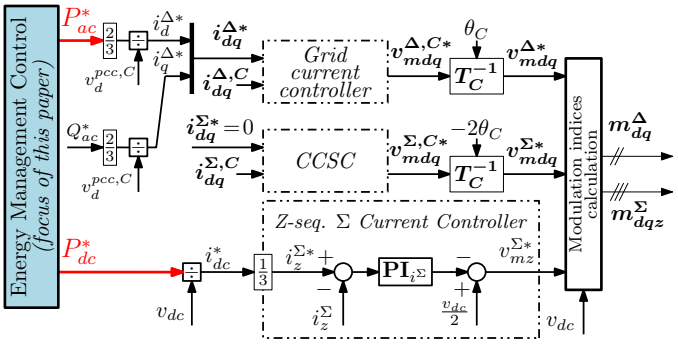

Fig. 5. *Energy-based* controller for reference SSTI-MMC model from Fig. 3 – AC and DC power references in red (More details in [18]).

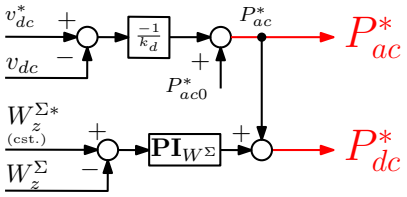

Fig. 6. Energy Management Control # 1: Energy control via DC power with constant reference used in [18].

2) Energy-based controller structure: The global control structure is shown in Fig. 5. It is based on the Circulating Current Suppressing Controller (CCSC) from [24] and the independent control of the AC and DC powers (P_{ac} and P_{dc}) with an *Energy management control* block which is the main focus of this paper and it is further detailed. The grid current controller is a generic synchronous PI dq control with crossed decoupling feed-forward terms "$\omega L \boldsymbol{i^{\Delta}_{dq}}$" and $\boldsymbol{v^{pcc}_{dq}}$.

Note that the outputs of the grid current controllers and the CCSC (i.e. $\boldsymbol{v^{\Delta,C*}_{mdq}}$, $\boldsymbol{v^{\Sigma,C*}_{mdq}}$) are respectively transformed from the $\boldsymbol{dq^C}$ axes back to the *physical* $\boldsymbol{dq}$ frame with $\boldsymbol{T_C^{-1}}$. The modulation indices $\boldsymbol{m^{\Delta}_{dq}}$ and $\boldsymbol{m^{\Sigma}_{dqz}}$ are obtained acording to the Un-Compensated Modulation tehcnique (UCM) adopted in [17], i.e. dividing each modulated voltage reference by v_{dc}.

3) Energy Management Control #1: Energy controller via DC power with constant reference: In Fig. 6, the dedicated energy controller which regulates the total MMC energy to a constant level is given [18]. As a common practice, the energy reference $W_z^{\Sigma *}$ is set to 1 pu: this means that, in average, the voltages of the six arm equivalent capacitors are maintained close to 1 pu regardless of the DC voltage at the PCC-DC.

The AC power reference P^*_{ac} is obtained through the output of the DC voltage droop controller (with gain k_d) and the set-point P^*_{ac0} provided by the Transmission System Operators (TSO). The DC power reference P^*_{dc} is obtained by the sum of the output from the energy controller and P^*_{ac} sent as a feed-forward action to improve the dynamic response.

4) Simplified energetic analysis of energy-based controlled MMC on DC bus dynamics: From Fig. 2, the energy stored on the DC capacitor (W_{dc}) depends on the power exchanged by the MMC with the DC bus (P_{dc}) and the power flowing from the DC-grid (P_l) as expressed in (6), where it is assumed that $P_{dc} = P^*_{dc}$ for analysis purposes [14].

$$\frac{dW_{dc}}{dt} = \frac{1}{2} C_{dc} \frac{dv_{dc}^2}{dt} = P_l - P^*_{dc} \tag{6}$$

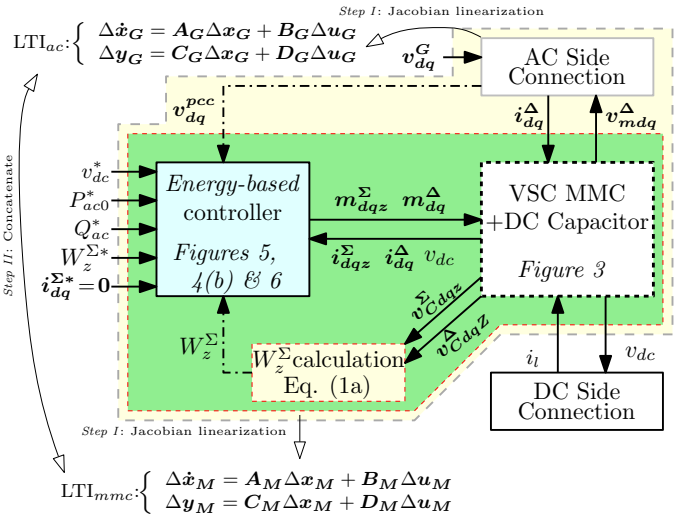

Fig. 7. Model of MMC with *Energy-based* controller, DC capacitor and AC grid.

Assuming also that $P_{ac} = P^*_{ac}$, the approximated dynamics of the energy stored on the MMC (W_z^{Σ}) are given in (7).

$$\frac{dW_z^{\Sigma}}{dt} \approx \frac{1}{2} C_{mmc} \frac{d(v_{Cz}^{\Sigma})^2}{dt} \approx P^*_{dc} - P^*_{ac} \tag{7}$$

Replacing P^*_{dc} from (7) into (6) yields:

$$\frac{1}{2} C_{dc} \frac{dv_{dc}^2}{dt} + \frac{1}{2} C_{mmc} \frac{d(v_{Cz}^{\Sigma})^2}{dt} = P_l - P^*_{ac} \tag{8}$$

Assuming an ideal energy controller (i.e. $W_z^{\Sigma} = W_z^{\Sigma *}$), it is implied that $v_{Cz}^{\Sigma} = v_{Cz}^{\Sigma *}$, where $v_{Cz}^{\Sigma *} = \sqrt{(2W_z^{\Sigma *}/C_{mmc})}$. Consequently, if $W_z^{\Sigma *}$ is constant, the term $d(v_{Cz}^{\Sigma})^2/dt$ from (8) is equal to zero. With this consideration, (8) results in (9).

$$\frac{1}{2} \underbrace{C_{dc}}_{C_{eff}} \frac{dv_{dc}^2}{dt} = P_l - P_{ac} \tag{9}$$

Equation (9) shows that the effective capacitance seen from the DC side (C_{eff}) is only considering the equivalent cable capacitance (C_{dc}). This simplified analysis is fundamental to understand the main issues when decoupling the MMC energy with the DC bus in MTDC systems: the voltage dynamics are mainly governed by the equivalent DC grid capacitance [12].

D. LTI model of a single MMC

The LTI model of a MMC with energy controller interacting with a MTDC grid is shown in Fig. 7, where the input-output relations are highlighted. The algebraic equation used for the W_z^{Σ} calculation is given in (1a).

In order to obtain the complete LTI model of the MMC from Fig. 7, two steps are followed. *Step I* consists in dividing the MMC model in two linear sub-models: LTI$_{ac}$ and LTI$_{mmc}$, where each one is linearized by means of the Jacobian linearization [25] and the states, inputs and selected outputs of both state-space linear systems are given in (10) for LTI$_{ac}$ and (11) for LTI$_{mmc}$ (the state variables $\xi_{\text{"x"}}$ correspond to the integral part of the controller for state "x").

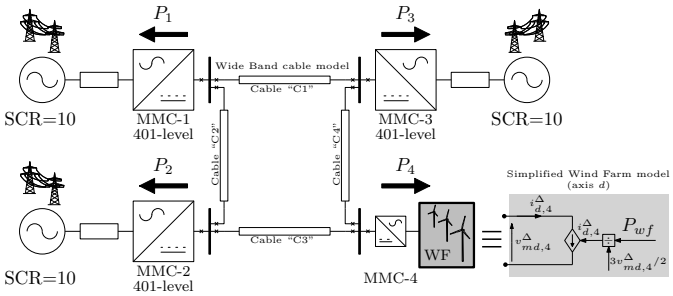

Fig. 8. Four terminal MTDC grid non-linear EMT *Simulation model*.

$$\boldsymbol{x_G} = [i_d^{\Delta}\ i_q^{\Delta}]^\top \in \mathbb{R}^2 \tag{10a}$$

$$\boldsymbol{u_G} = [v_{md}^{\Delta}\ v_{mq}^{\Delta}\ v_d^{G}\ v_q^{G}]^\top \in \mathbb{R}^4 \tag{10b}$$

$$\boldsymbol{y_G} = [\boldsymbol{x_G}^\top\ v_d^{pcc}\ v_q^{pcc}]^\top \in \mathbb{R}^4 \tag{10c}$$

$$\boldsymbol{x_M} = [\underbrace{\theta_C\ \xi_{pll}\ \boldsymbol{\xi}_{\boldsymbol{i}_{\boldsymbol{dq}}^{\boldsymbol{\Delta}}}}_{\text{Controllers}}^\top\ \underbrace{\boldsymbol{\xi}_{\boldsymbol{i}_{\boldsymbol{dq}}^{\boldsymbol{\Sigma}}}}^\top\ \xi_{W_z^{\Sigma}}\ \underbrace{\boldsymbol{i}_{\boldsymbol{dqz}}^{\boldsymbol{\Sigma}}}^\top\ \boldsymbol{v}_{\boldsymbol{Cdqz}}^{\boldsymbol{\Sigma}}{}^\top\ \boldsymbol{v}_{\boldsymbol{CdqZ}}^{\boldsymbol{\Delta}}{}^\top}_{\text{MMC}}\ \underbrace{v_{dc}}_{\text{DC bus}}]^\top \in \mathbb{R}^{18} \tag{11a}$$

$$\boldsymbol{u_M} = [\underbrace{v_{dc}^*\ W_z^{\Sigma *}\ P_{ac0}^*\ Q_{ac}^*\ \boldsymbol{i}_{\boldsymbol{dq}}^{\boldsymbol{\Sigma *}}}^\top_{\text{Controller Set-Points}}\ \underbrace{\boldsymbol{v}_{\boldsymbol{dq}}^{\boldsymbol{pcc}}}^\top\ \underbrace{\boldsymbol{i}_{\boldsymbol{dq}}^{\boldsymbol{\Delta}}}^\top_{\text{AC side}}\ \underbrace{i_l}_{\text{DC side}}]^\top \in \mathbb{R}^{11} \tag{11b}$$

$$\boldsymbol{y_M} = [\boldsymbol{x_M}^\top\ v_{md}^{\Delta}\ v_{mq}^{\Delta}]^\top \in \mathbb{R}^{20} \tag{11c}$$

Step II merges both LTI sub-models with the methodology explained in [26], leading to a single LTI representation which gathers the MMC, controller and the AC grid as shown in (12). The states and inputs of the concatenated LTI system are given in (13), where the symbol "||" represents the concatenation.

$$\begin{cases} \Delta\dot{\boldsymbol{x}}_{\boldsymbol{M\|G}} = \boldsymbol{A}_{\boldsymbol{M\|G}}\Delta\boldsymbol{x}_{\boldsymbol{M\|G}} + \boldsymbol{B}_{\boldsymbol{M\|G}}\Delta\boldsymbol{u}_{\boldsymbol{M\|G}} \\ \Delta\boldsymbol{y}_{\boldsymbol{M\|G}} = \boldsymbol{C}_{\boldsymbol{M\|G}}\Delta\boldsymbol{x}_{\boldsymbol{M\|G}} + \boldsymbol{D}_{\boldsymbol{M\|G}}\Delta\boldsymbol{u}_{\boldsymbol{M\|G}} \end{cases} \tag{12}$$

$$\boldsymbol{x_{M\|G}} = [\boldsymbol{x_M}^\top\ \boldsymbol{x_G}^\top]^\top \in \mathbb{R}^{20} \tag{13a}$$

$$\boldsymbol{u_{M\|G}} = [\underbrace{v_{dc}^*\ W_z^{\Sigma *}\ P_{ac0}^*\ Q_{ac}^*\ \boldsymbol{i}_{\boldsymbol{dq}}^{\boldsymbol{\Sigma *}}}^\top_{\text{Controller Set-Points}}\ \underbrace{\boldsymbol{v}_{\boldsymbol{dq}}^{\boldsymbol{G}}}^\top_{\text{AC side}}\ \underbrace{i_l}_{\text{DC side}}]^\top \in \mathbb{R}^9 \tag{13b}$$

III. MMC-Based MTDC Modeling and Analysis

In this section, the MMC model from previous section is used for creating a four-terminal MTDC grid.

A. EMT Simulation model of MMC-based MTDC grid

The four terminal MMC-based MTDC grid considered in this paper is shown in Fig. 8. In the EMT *Simulation model* used as a reference, the MMCs are modeled with the switching "Model #2: *Equivalent Circuit-Based Model*" with 400 sub-modules per arm from [19] and the reduced switching-frequency capacitor balancing algorithm from [24]. Converters MMC-1, MMC-2 and MMC-3 are connected to onshore AC grids (with SCR equal to 10) and they are equipped with DC voltage droop controllers. The DC grid is composed by four cables with equal length (70 km), namely "$C1$", "$C2$", "$C3$" and "$C4$", with detailed Wide Band cable models whose parameters are given in [27]. The chosen cable length is in accordance with real HVDC offshore projects [28].

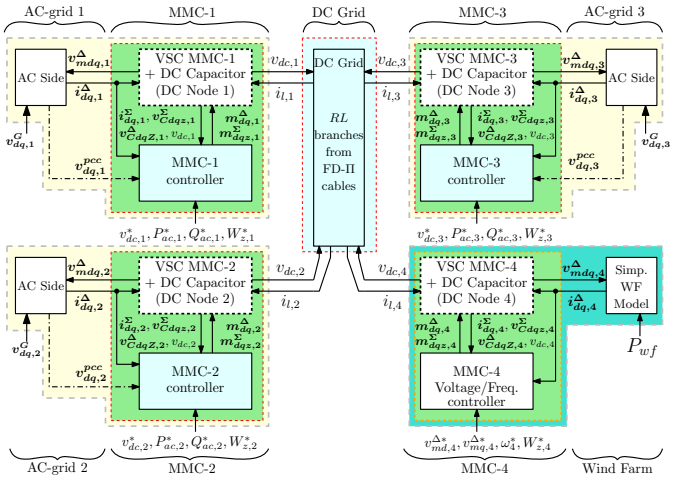

Fig. 9. SSTI model equations of MMC-based MTDC grid for linearization.

The model of the Wind Farm (WF) is much simplified and assumed to be a simple power injector (P_{wf}) as depicted in Fig. 8 without losing generality, since this study considers the abrupt disconnection of the WF. The AC-side control of MMC-4 modulates the AC voltage with $v_{md}^{\Delta *}=1$ pu and $v_{mq}^{\Delta *}=0$ pu and a frequency ω^*.

B. LTI modeling of MMC-based MTDC grids

The LTI model of the MTDC grid is obtained following a step-by-step methodology, where the overall state-space representation of the system is obtained by the concatenation of previously linearized sub-systems (DC grid, AC grids and MMCs with their controllers). The whole system is shown in Fig. 9 and the main steps for obtaining the state-space linear representation (LTI model) are discussed in the following.

• **Step 1: Creation of DC grid in state-space representation:** Each cable is modeled with the *Frequency Dependent-PI* from [27], with three parallel branches per cable. This model is linear by nature since it is composed only by RL components (the endpoint capacitors are considered in the converter models as in [27] without losing generality). The DC grid LTI model is shown in (14), and the states and inputs are given in (15), where $\boldsymbol{i}_{\boldsymbol{L,123}}^{\boldsymbol{Cj}} = [i_{L,1}^{Cj}\ i_{L,2}^{Cj}\ i_{L,3}^{Cj}]^\top$ represents the currents in the j-th FD-Π cable model.

$$\begin{cases} \Delta\dot{\boldsymbol{x}}_{\boldsymbol{dc}} = \boldsymbol{A}_{\boldsymbol{dc}}\Delta\boldsymbol{x}_{\boldsymbol{dc}} + \boldsymbol{B}_{\boldsymbol{dc}}\Delta\boldsymbol{u}_{\boldsymbol{dc}} \\ \Delta\boldsymbol{y}_{\boldsymbol{dc}} = \boldsymbol{C}_{\boldsymbol{dc}}\Delta\boldsymbol{x}_{\boldsymbol{dc}} + \boldsymbol{D}_{\boldsymbol{dc}}\Delta\boldsymbol{u}_{\boldsymbol{dc}} \end{cases} \tag{14}$$

$$\boldsymbol{x_{dc}} = [\boldsymbol{i}_{\boldsymbol{L,123}}^{\boldsymbol{C1}}{}^\top\ \boldsymbol{i}_{\boldsymbol{L,123}}^{\boldsymbol{C2}}{}^\top\ \boldsymbol{i}_{\boldsymbol{L,123}}^{\boldsymbol{C3}}{}^\top\ \boldsymbol{i}_{\boldsymbol{L,123}}^{\boldsymbol{C4}}{}^\top]^\top \in \mathbb{R}^{12} \tag{15a}$$

$$\boldsymbol{u_{dc}} = [v_{dc,1}\ v_{dc,2}\ v_{dc,3}\ v_{dc,4}]^\top \in \mathbb{R}^4 \tag{15b}$$

$$\boldsymbol{y_{dc}} = [i_{l,1}\ i_{l,2}\ i_{l,3}\ i_{l,4}]^\top \in \mathbb{R}^4 \tag{15c}$$

• **Step 2: Creation of LTI models of MMCs with DC capacitor and controllers in state-space representation:** Each converter is modeled and linearized as discussed in Section II-D. However, the DC capacitance C_{dc} from Fig. 2 is now the sum of the capacitors of each cable connected at a given PCC-DC. Also, the current i_l reaching towards this equivalent capacitor (see (13b)) is now provided by the sum

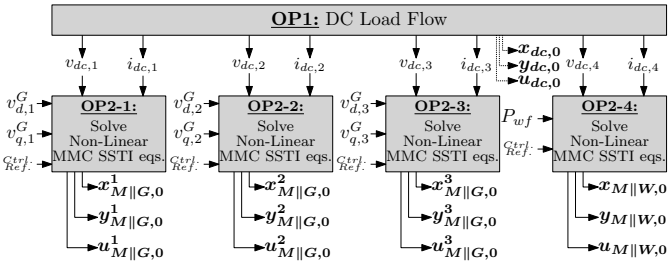

Fig. 10. The two step process to calculate the MTDC Operating Point.

of the cable inductors connected to the converter n, namely $i_{l,n}$. The model of MMC-4 and the associated wind-farm is modeled in a similar way as the rest of the converters, and the LTI model is shown in (16) and (17) noted as "$M\|W$".

$$\begin{cases} \Delta\dot{\boldsymbol{x}}_{M\|W} = \boldsymbol{A}_{M\|W}\Delta\boldsymbol{x}_{M\|W} + \boldsymbol{B}_{M\|W}\Delta\boldsymbol{u}_{M\|W} \\ \Delta\boldsymbol{y}_{M\|W} = \boldsymbol{C}_{M\|W}\Delta\boldsymbol{x}_{M\|W} + \boldsymbol{D}_{M\|W}\Delta\boldsymbol{u}_{M\|W} \end{cases} \tag{16}$$

$$\boldsymbol{x}_{M\|W} = [\boldsymbol{\xi}_{i^{\Sigma}_{dq,4}}^{\top}\ \xi_{W^{\Sigma}_{z,4}}\ \boldsymbol{i}^{\boldsymbol{\Sigma}}_{\boldsymbol{dqz,4}}{}^{\top}\ \boldsymbol{v}^{\boldsymbol{\Sigma}}_{\boldsymbol{Cdqz,4}}{}^{\top}\ \boldsymbol{v}^{\boldsymbol{\Delta}}_{\boldsymbol{CdqZ,4}}{}^{\top}\ v_{dc,4}]^{\top} \in \mathbb{R}^{14} \tag{17a}$$

$$\boldsymbol{u}_{M\|W} = [\boldsymbol{v}^{\boldsymbol{\Delta}*}_{\boldsymbol{mdq,4}}\ \omega_4^*\ W^{\Sigma*}_{z,4}\ \boldsymbol{i}^{\boldsymbol{\Sigma}*}_{\boldsymbol{dq,4}}{}^{\top}\ \boldsymbol{i}^{\boldsymbol{\Delta}}_{\boldsymbol{dq,4}}{}^{\top}\ i_{l,4}\ P_{wf}]^{\top} \in \mathbb{R}^{10} \tag{17b}$$

$$\boldsymbol{y}_{M\|W} = \boldsymbol{x}_{M\|W} \in \mathbb{R}^{14} \tag{17c}$$

• **Step 3: Calculation of Operating Point (OP):** A DC load flow calculation is used to obtain all the DC voltages and currents at each PCC-DC (**OP1**). This information is used to solve the non-linear equations of each MMC-SSTI in a step-by-step process as illustrated in Fig. 10 (**OP2**).

• **Step 4: Concatenation of linear subsystems:** Once the solutions of the operating point are obtained, it is possible to obtain numerically the matrices $\boldsymbol{A}_{M\|G}$, $\boldsymbol{B}_{M\|G}$, $\boldsymbol{C}_{M\|G}$ and $\boldsymbol{D}_{M\|G}$ of each MMC-LTI model (see (12)), and then combined into a single state-space global representation with the MMC-4, WF and DC grid as shown in (18). The MTDC states $\boldsymbol{x}_{\boldsymbol{mtdc}}$ and inputs $\boldsymbol{u}_{\boldsymbol{mtdc}}$ are shown in (19), where $\boldsymbol{x}^{\boldsymbol{m}}_{\boldsymbol{M\|G}}$ represents the states from (13a) for the MMC-m and their AC grids.

$$\begin{cases} \Delta\dot{\boldsymbol{x}}_{\boldsymbol{mtdc}} = \boldsymbol{A}_{\boldsymbol{mtdc}}\Delta\boldsymbol{x}_{\boldsymbol{mtdc}} + \boldsymbol{B}_{\boldsymbol{mtdc}}\Delta\boldsymbol{u}_{\boldsymbol{mtdc}} \\ \Delta\boldsymbol{y}_{\boldsymbol{mtdc}} = \boldsymbol{C}_{\boldsymbol{mtdc}}\Delta\boldsymbol{x}_{\boldsymbol{mtdc}} + \boldsymbol{D}_{\boldsymbol{mtdc}}\Delta\boldsymbol{u}_{\boldsymbol{mtdc}} \end{cases} \tag{18}$$

$$\boldsymbol{x}_{\boldsymbol{mtdc}} = [\boldsymbol{x}_{\boldsymbol{dc}}^{\top}\ \boldsymbol{x}^{\boldsymbol{1}}_{\boldsymbol{M\|G}}{}^{\top}\ \boldsymbol{x}^{\boldsymbol{2}}_{\boldsymbol{M\|G}}{}^{\top}\ \boldsymbol{x}^{\boldsymbol{3}}_{\boldsymbol{M\|G}}{}^{\top}\ \boldsymbol{x}_{M\|W}{}^{\top}]^{\top} \in \mathbb{R}^{86} \tag{19a}$$

$$\begin{aligned} \boldsymbol{u}_{\boldsymbol{mtdc}} = [& \underbrace{v^*_{dc,1}\ W^{\Sigma*}_{z,1}\ P^*_{ac0,1}\ Q^*_{ac,1}\ \boldsymbol{i}^{\boldsymbol{\Sigma}*}_{\boldsymbol{dq,1}}{}^{\top}\ \boldsymbol{v}^{\boldsymbol{G}}_{\boldsymbol{dq,1}}{}^{\top}}_{\text{MMC-1}} \dots \\ & \underbrace{\dots v^*_{dc,2}\ W^{\Sigma*}_{z,2}\ P^*_{ac0,2}\ Q^*_{ac,2}\ \boldsymbol{i}^{\boldsymbol{\Sigma}*}_{\boldsymbol{dq,2}}{}^{\top}\ \boldsymbol{v}^{\boldsymbol{G}}_{\boldsymbol{dq,2}}{}^{\top}}_{\text{MMC-2}} \dots \\ & \underbrace{\dots v^*_{dc,3}\ W^{\Sigma*}_{z,3}\ P^*_{ac0,3}\ Q^*_{ac,3}\ \boldsymbol{i}^{\boldsymbol{\Sigma}*}_{\boldsymbol{dq,3}}{}^{\top}\ \boldsymbol{v}^{\boldsymbol{G}}_{\boldsymbol{dq,3}}{}^{\top}}_{\text{MMC-3}} \dots \\ & \underbrace{\dots v^{\Delta*}_{md,4}\ v^{\Delta*}_{mq,4}\ \omega_4^*\ W^{\Sigma*}_{z,4}\ \boldsymbol{i}^{\boldsymbol{\Sigma}*}_{\boldsymbol{dq,4}}{}^{\top}\ P_{wf}}_{\text{MMC-4 and WF}}]^{\top} \in \mathbb{R}^{31} \end{aligned} \tag{19b}$$

In the following, the obtained LTI model (18) is used for the dynamic analysis of MMC-based MTDC grids.

Table II
DC LOAD FLOW — BASE VALUES: 1000 MW; 640 KV

Station	Nominal power [MW]	P_{dc} [pu]	v_{dc} [pu]
MMC-1	1200	1.193	1.0000
MMC-2	1000	0.400	1.0017
MMC-3	1000	−0.600	1.0041
MMC-4	1000	$P_{dc} = -0.993$, $P_{wf} = -1$	1.0053

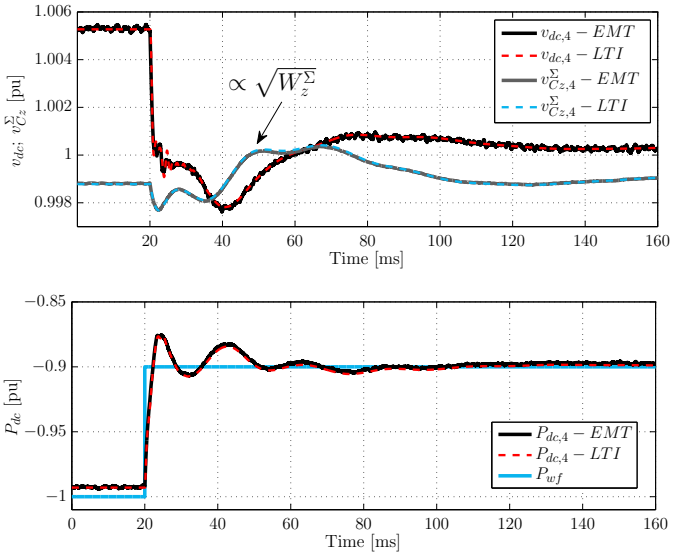

Fig. 11. Small-signal scenario: Comparison of time-domain simulations of EMT and small-signal model (LTI) of a four terminal MTDC grid - Converters are equipped with *Energy-based* controllers with constant energy references.

1) Time Domain Validation: In order to validate the small-signal modeling approach, two time-domain simulations are performed with the EMT model of the MTDC grid in EMTP-RV from Fig. 8 and the small-signal model from (18) with Matlab/Simulink: small-signal and large-signal scenario. The simulation cases start with a DC load flow provided in Table II (note that P_{dc} for MMC-4 is not exactly the same as P_{wf}, which is measured on its AC-side). The droop parameters k_d for each converter are set to 0.15 pu, for having an allowed ± 0.05 pu of DC voltage deviation around the operating point for a total loss of 1 pu of power imbalance on the DC grid. The arm capacitor voltages v^{Σ}_{Cz} are set to 1 pu due to the constant energy reference. The response times for the inner current controllers ($\boldsymbol{i}^{\boldsymbol{\Delta}}_{\boldsymbol{dq}}$, $\boldsymbol{i}^{\boldsymbol{\Sigma}}_{\boldsymbol{dqz}}$) are set to 5 ms, while the energy controllers are set to 50 ms. The main MMC and cable parameters are gathered in the Appendix A.

For the small-signal scenario, the WF power is reduced in 0.1 pu at $t = 20$ ms. Simulation results for the DC voltage v_{dc}, arm capacitor voltage v^{Σ}_{Cz}, DC power P_{dc} and WF power P_{wf} for MMC-4 are shown in Fig. 11. As observed in the results, the LTI model reproduces accurately the system response. For the rest of variables, no noticeable discrepancy is observed.

For the large-signal scenario, the WF is disconnected at $t = 20$ ms, manifesting a sudden reduction of 1 pu of wind power production P_{wf}. Simulation results for the DC voltages for MMC-1 and MMC-4, arm capacitor voltage v^{Σ}_{Cz} for MMC-1, and DC powers are shown in Fig. 12. The voltages for

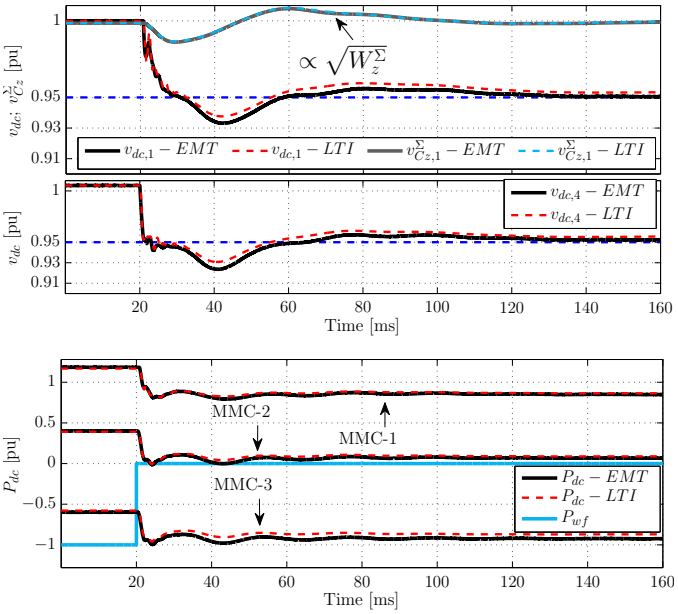

Fig. 12. Large-signal scenario: Comparison of time-domain simulations of EMT and small-signal model (LTI) of a four terminal MTDC grid - Converters are equipped with *Energy-based* controllers with constant energy references.

MMC-2 and MMC-3 behave similarly as for MMC-1.

As observed, the abrupt step on P_{wf} causes a severe transient behavior on $v_{dc,4}$, and the ± 0.05 pu limit on the DC voltage is easily violated for all the terminals, which is not desired, as it causes aging and requires an oversizing of High-Voltage components [29].

2) Singular Value Decomposition (SVD): The SVD method may be considered as an effective tool for the analysis of Multi-Inputs and Multi-Outputs (MIMO) systems, which is equivalent to the transfer function approach for Single-Input and Single-Output (SISO) systems [30], [31]. Indeed, since the studied MTDC grid is a MIMO system, the SVD method is suitable for its frequency analysis [3]. In this paper, the focus is given to the evolution of the variables $v_{dc,m}$ and $v^{\Sigma}_{Cz,m}$ with respect to the variation of the WF power deviation ΔP_{wf}, so two different Single-Input Multi-Output transfer functions (SIMO) are considered: first, the function $\boldsymbol{G_1}(s)$ is focused on the evolution of the DC voltage deviation of the four stations with respect to ΔP_{wf}, so $\boldsymbol{y_{G_1}} = [\Delta v_{dc,1}\ \Delta v_{dc,2}\ \Delta v_{dc,3}\ \Delta v_{dc,4}]^{\top}$ and $u_{G_1} = \Delta P_{wf}$. Second, the function $\boldsymbol{G_2}(s)$ considers the voltage deviations on the arm capacitor voltages of MMC-1, MMC-2 and MMC-3 also with respect to ΔP_{wf}, so $\boldsymbol{y_{G_2}} = \left[\Delta v^{\Sigma}_{Cz,1}\ \Delta v^{\Sigma}_{Cz,2}\ \Delta v^{\Sigma}_{Cz,3}\ \Delta v^{\Sigma}_{Cz,4}\right]^{\top}$ and $u_{G_2} = \Delta P_{wf}$.

The study aims at determining if the DC voltage deviation or the arm capacitor voltages of each converter station (the outputs $\boldsymbol{y_{G_1}}$ and $\boldsymbol{y_{G_2}}$) are maintained within the acceptable range, which is set to $\pm 5\%$ for any power reference change of the WF (the input u_{G_1} and u_{G_2}), both from a static and a dynamic point of view. This limit is selected based on [2], [32]. The maximum allowable voltages deviation and the maximum possible power reference change of the converters can then be represented as a gain boundary in the frequency response of the MTDC system. In fact, by ensuring that the maximum

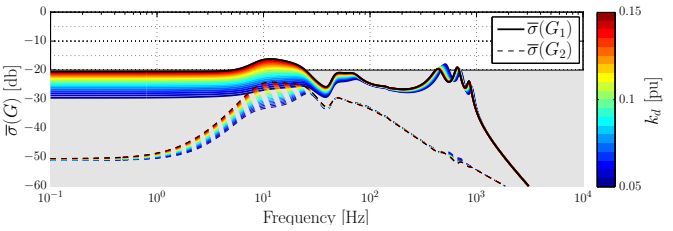

Fig. 13. SVD results for a sweep of the droop gain k_d of the MMCs – Constant energy reference for onshore MMCs — $P_{wf} = -1$ pu.

singular value $\overline{\sigma}$ does not bypass the gain boundaries corresponding to the voltage deviation, the linear MTDC system is assured to comply with the imposed constraint [33].

The boundary for a maximum allowed deviation of the DC voltages $\Delta v^{\max}_{dc}$ or arm capacitor voltages $\Delta v^{\Sigma\max}_{Cz}$ of 5% with respect to a power variation of the WF $\Delta P^{\text{dev}}_{wf}$ of 1 pu is given by (20):

$$\underbrace{20\log_{10}\left(\frac{\sqrt{\sum_{i=1}^{4}\left(\Delta v^{\max}_{dc,i}\right)^2}}{\sqrt{\left(\Delta P^{\text{dev}}_{wf}\right)^2}}\right)}_{\text{Limit for } \boldsymbol{G_1}(s)} = \underbrace{20\log_{10}\left(\frac{\sqrt{\sum_{i=1}^{4}\left(\Delta v^{\Sigma\max}_{Cz,i}\right)^2}}{\sqrt{\left(\Delta P^{\text{dev}}_{wf}\right)^2}}\right)}_{\text{Limit for } \boldsymbol{G_2}(s)} = -20 \text{ dB} \qquad (20)$$

In Fig. 13, the results for a sweep of the droop gain k_d of all MMCs at the same time are shown (the stability has been verified for all the sweep). Since the SVD results for $\boldsymbol{G_1}(s)$ and the considered parameters are crossing the -20 dB boundary defined in (20) when the droop parameters approach to 0.15 pu, it implies that the DC voltages are violating the $\pm 5\%$ for certain frequencies of the input P_{wf} (which are easily excited in transients). Only for low values of k_d the DC voltage dynamics may be guaranteed, but it may increase the potential risk of interactions with the AC-side and the stress on the high-voltage equipment. This demonstrates that only the tuning of k_d is not sufficient to guarantee an acceptable damping for the system. With respect to the SVD from $\boldsymbol{G_2}(s)$, MMC capacitor voltages are well maintained within the limits, due to the constant energy references.

In the following sections, an in-depth analysis is carried out to improve the SVD results and hence, the dynamic behavior of the DC voltages in MMC-based MTDC grids.

IV. Energy Management Control Variants

Two different variants are now considered and analyzed for the energy management control from Fig. 5: the Virtual Capacitor Control from [14], and a novel derivative control.

A. Energy Management Control #2: Coupled MMC energy with DC bus with Virtual Capacitor Control from [14]

In this strategy, the Energy management control in Fig. 5 is slightly modified for enabling the participation of the internal energy on the DC bus voltage dynamics. This is performed with an appropriated modification on the energy reference as:

$$W^{\Sigma *}_z = \frac{1}{2}\underbrace{KC_{mmc}}_{\text{Virtual Capacitor}}\left(v^2_{dc} - v^2_{dc0}\right) + W^{\Sigma *}_{z0} \qquad (21)$$

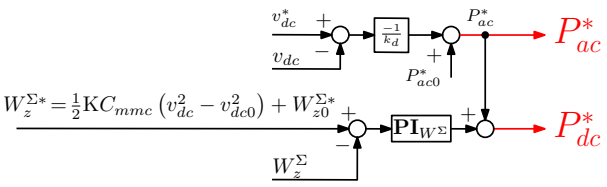

Fig. 14. Energy Management Control # 2: *Virtual Capacitor* control [14].

where v_{dc0} corresponds to the steady-state value of the DC voltage and $W_{z0}^{\Sigma*}$ is the desired initial stored energy. The parameter K is referred as "Capacitor Coefficient" and defines how much of the energy W_z^Σ varies according to the DC voltage deviation. Now, the arm capacitors voltage reference $v_{Cz}^{\Sigma*}$ can be related to the energy reference as:

$$v_{Cz}^{\Sigma*} \approx \sqrt{\frac{2W_z^{\Sigma*}}{C_{mmc}}} = \sqrt{\mathrm{K}\left(v_{dc}^2 - v_{dc0}^2\right) + W_{z0}^{\Sigma*}} \qquad (22)$$

As in Section II-C4, the effective DC bus capacitance C_{eff} is recalculated: substituting (22) into (8) and taking into account a perfect energy controller (i.e. assuming that $v_{Cz}^\Sigma = v_{Cz}^{\Sigma*}$), it yields:

$$\frac{1}{2}\underbrace{\left(C_{dc} + \mathrm{K}C_{mmc}\right)}_{C_{eff}}\frac{dv_{dc}^2}{dt} = P_l - P_{ac}^* \qquad (23)$$

As shown in (23), the effective DC bus capacitance C_{eff} considers C_{dc} and also K times the total MMC capacitance.

The implementation of the Energy Management Control #2: *Virtual Capacitor* control is shown in Fig. 14.

1) Time domain simulations: For evaluating the energy management strategy, the same large-signal time domain simulation as in Section III-B1 is performed. The energy references for converters MMC-1, MMC-2 and MMC-3 are given by (21), with $\mathrm{K} = 1.5$, while maintaining the constant energy reference for MMC-4 attached to the WF. The LTI model of the MTDC is re-generated taking into account the modification on the energy reference with (21). Simulation results for the DC power and voltages are gathered in Fig. 15. The DC voltages at each converter are now maintained under the $\%5$ limit.

2) Limitations of Virtual Capacitor Control in droop-controlled MTDC grids: The DC voltages are near their nominal values only when a dedicated master controller sets the proper references for regulating the DC power flow. In case of transients causing a power imbalance, the DC voltage experiences a deviation due to the proportional droop controllers. Consequently, the term $v_{dc}^2 - v_{dc0}^2$ in (21) is not zero, so a deviation on the energy is expected for the steady state condition after an event (as it can be observed in the arm capacitor voltages v_{Cz}^Σ in Fig. 15). This difference on the energy level will exist until a dedicated master controller regulates again the stored energy.

This characteristic can be seen on the SVD from Fig. 16, where a parametric sweep of K is performed (from $\mathrm{K} = 1$ up to 2.4 for each MMC onshore). The SVD from $\boldsymbol{G_1}$ shows that by increasing the value of K, the low frequency behavior of the MTDC is attenuated (as the stored energy is virtually increased). However, the SVD from $\boldsymbol{G_2}$ shows that the final

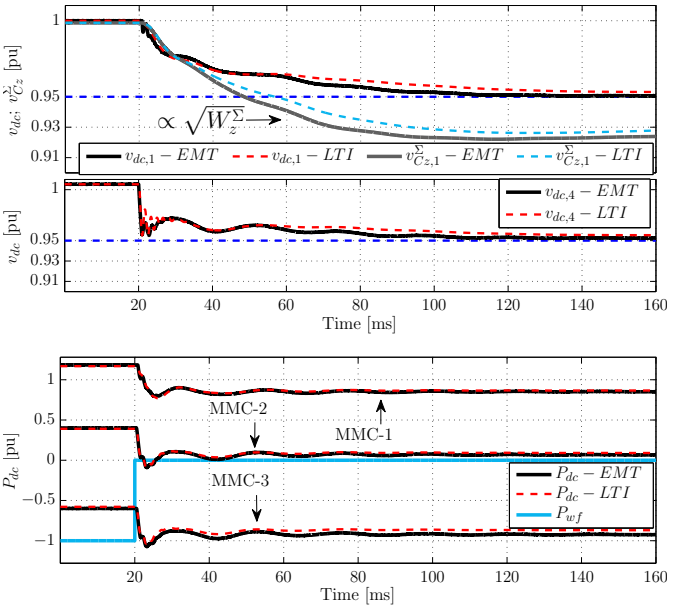

Fig. 15. Comparison of time-domain simulations of EMT and small-signal model (LTI) of a four terminal MTDC grid - Converters are equipped with *Energy-based* controllers with the *Virtual Capacitor* control ($\mathrm{K} = 1.5$, $k_d = 0.15$ pu).

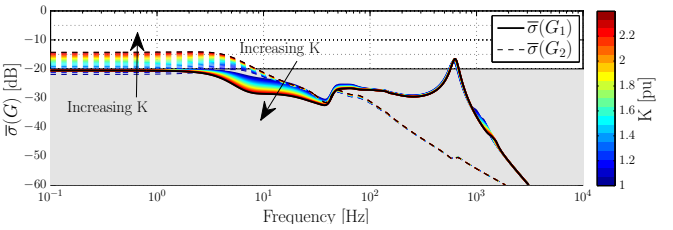

Fig. 16. SVD results for a sweep of K - *Virtual Capacitor* control - $\boldsymbol{G_1}$: Input $\boldsymbol{u} = P_{wf}$, Outputs $\boldsymbol{y} = [v_{dc,1}\ v_{dc,2}\ v_{dc,3}\ v_{dc,4}]^\top$; $\boldsymbol{G_2}$: Input $\boldsymbol{u} = P_{wf}$, Outputs $\boldsymbol{y} = [v_{Cz,1}^\Sigma\ v_{Cz,2}^\Sigma\ v_{Cz,3}^\Sigma]^\top$ — $P_{wf} = -1$ pu, $k_d = 0.15$ pu.

deviation of the arm capacitor voltages are compromised when the capacitor coefficient K is increased. If the energy deviation is excessive (hence, the arm capacitor voltages are heavily discharged), there is a potential risk of hitting the converter limits since the arm capacitor voltages has such a low value, that it is not possible to form the desired arm voltage needed for the proper operation of the converter.

This phenomenon makes the choice of K a complicated task since several limitations should be taken into account. In the following section, a different approach for controlling the DC bus voltage while keeping the concept of energy sharing is given, which overcomes these limitations.

B. Energy Management Control #3: DC Power Derivative Control

Contrary to what has been shown in Figs. 6 and 14, another feasible arrangement could be to control the MMC internal energy with P_{ac}^* and the DC voltage with P_{dc}^* [34]. Doing so, it is possible to add a derivative term with respect to "$(\mathrm{K}C_{mmc}/2)v_{dc}^2$" to the DC power reference generation P_{dc}^*

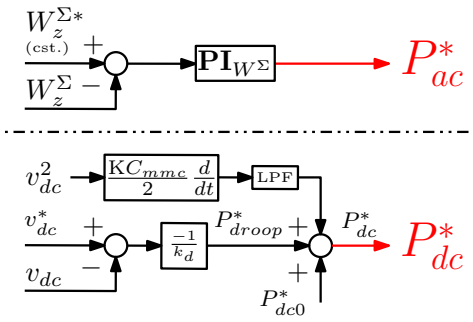

Fig. 17. Energy Management Control # 3: Derivative control.

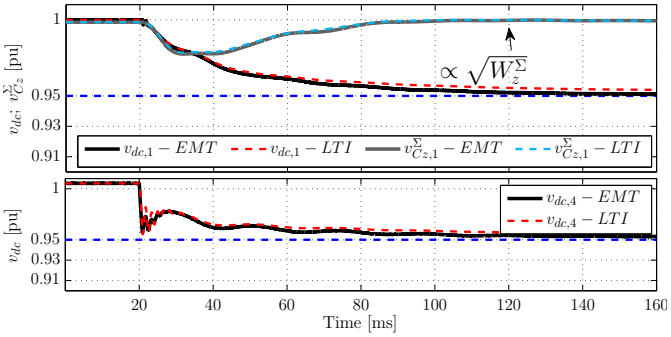

Fig. 18. Comparison of time-domain simulations of EMT and small-signal model (LTI) of a four terminal MTDC grid - Converters are equipped with *Energy-based* controllers with derivative control (K = 1.5).

(see (24a)) for obtaining the virtual capacitor effect from the Energy Management Control #2 as shown in (24b).

$$\frac{1}{2}C_{dc}\frac{dv_{dc}^2}{dt} = P_l - (P_{droop}^* + P_{dc0}^* + \underbrace{\frac{\mathrm{K}C_{mmc}}{2}\frac{dv_{dc}^2}{dt}}_{\text{Derivative term}}) \quad (24a)$$

$$\frac{1}{2}\underbrace{(C_{dc} + \mathrm{K}C_{mmc})}_{C_{eff}}\frac{dv_{dc}^2}{dt} = P_l - P_{droop}^* - P_{dc0}^* \quad (24b)$$

The Energy Management Control #3 is given in Fig. 17, where the main characteristic for this case is that the generation of P_{ac}^* and P_{dc}^* are inverted with respect to the previous strategies: the total energy is controlled via P_{ac}^*, while the droop-controller acts directly on the DC power reference P_{dc}^* in addition to the derivative term. Moreover, a washout filter (Low-Pass Filter (LPF) with a time constant of 1 ms) is added for overcoming the fast changes of the derivative action.

1) Time domain simulations: The same time domain simulation is performed as in previous Sections for the energy management strategy from Fig. 17, and results are shown in Fig. 18. Comparing the results from Fig. 18 with the waveforms from previous strategy in Fig. 15, it can be noticed that the DC voltages behave similarly.

2) Linear analysis: Results in Fig. 19 considering the derivative control show that the deviations of the arm capacitor voltages are not violated anymore for the same values of K.

C. Offshore converters participation on DC dynamics support

As observed throughout the different SVD results in this paper (Figs. 13, 16 and 19), the peak around 650 Hz is always present. The information given by the SVD is condensed in a single graph and the explanation of this resonance cannot be directly adjudicated to a part of the system without further analysis. In Fig. 20, results for the SVD from Fig. 19 with K = 2.4, and the individual transfer functions are shown highlighting that the aforementioned resonance is mostly related to the DC voltage of the converter connected to the WF (i.e. $v_{dc,4}(s)/P_{wf}(s)$). This resonance is inherent to the system and it cannot be attenuated by the control actions on the onshore MMCs. This is coherent with [10], where it is suggested that the WF could also participate on the DC dynamics support.

Indeed, the aforementioned improvement can be assessed with an appropriated Energy Management Control on the offshore converter as e.g. the Virtual Capacitor strategy discussed in Section IV-A (even if they are not equipped with droop controller). For exemplifying this concept, a parametric sweep of K of MMC-4 equipped with the Virtual Capacitor Control is performed, varying from 0 (constant energy reference) to 1 (contribution to the effective DC capacitance of C_{mmc}). The rest of the system is the same as for Fig. 20. Results are shown in Fig. 21, where it can be seen that for values of K > 0.2 on MMC-4, the dynamic response of the DC grid complies with imposed voltage limitations for all the frequency range.

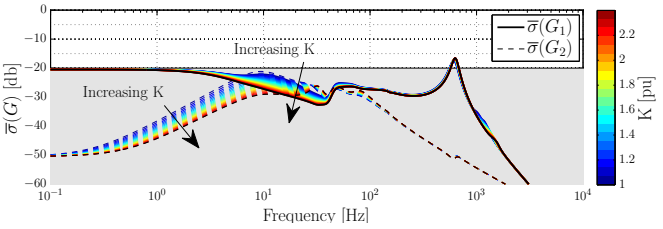

Fig. 19. SVD results for a sweep of K – Derivative control - $\boldsymbol{G_1}$: Input $\boldsymbol{u} = P_{wf}$, Outputs $\boldsymbol{y} = [v_{dc,1}\ v_{dc,2}\ v_{dc,3}\ v_{dc,4}]^\top$; $\boldsymbol{G_2}$: Input $\boldsymbol{u} = P_{wf}$, Outputs $\boldsymbol{y} = [v_{Cz,1}^{\Sigma}\ v_{Cz,2}^{\Sigma}\ v_{Cz,3}^{\Sigma}]^\top$ — $P_{wf} = -1$ pu.

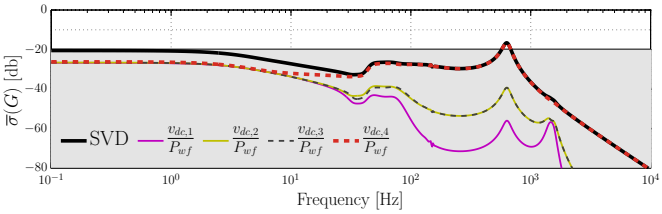

Fig. 20. SVD results for Derivative control with K = 2.4 - $\boldsymbol{G_1}$ and the individual transfer functions.

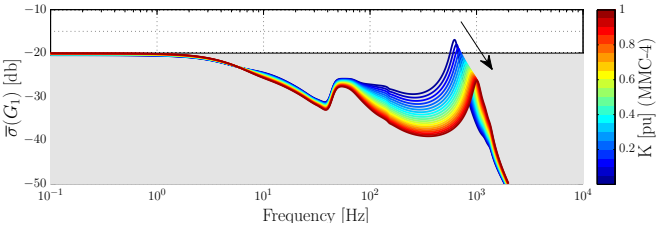

Fig. 21. Participation of offshore converter in DC bus dynamics improvement: SVD results for a sweep of K of MMC-4 with Virtual Capacitor Control (K = 2.4 for onshore converters) — $P_{wf} = -1$ pu.

Table III
CABLE PARAMETERS FOR THE FREQUENCY-DEPENDENT Π MODEL

	Parameter	Value	Parameter	Value
RL branch 1:	r_{z1}	$0.1265\ \Omega/km$	l_{z1}	0.2644 mH$/km$
RL branch 2:	r_{z2}	$0.1504\ \Omega/km$	l_{z2}	7.2865 mH$/km$
RL branch 3:	r_{z3}	$0.0178\ \Omega/km$	l_{z3}	3.6198 mH$/km$
Shunt elements:	g_y	$0.1015\ \mu\Omega^{-1}/km$	c_y	$0.16156\ \mu$F$/km$

Table IV
MMC PARAMETERS (τ_x, ζ_x: RESPONSE TIME AND DAMPING FOR VARIABLE "x")

Parameter	Value	Parameter	Value	Parameter	Value
U_{1n}	320 kV	R_f	$0.521\ \Omega$	τ_i^{Δ}	10 ms
P_n	See Table II	L_f	58.7 mH	τ_i^{Σ}	5 ms
v_{dcn}	640 kV	R_{arm}	$1.024\ \Omega$	τ_W^{Σ}	50 ms
C_{arm}	32.55μ F	L_{arm}	48 mH	$\zeta_i^{\Delta}, \zeta_i^{\Sigma}, \zeta_W^{\Sigma}$	0.7

V. CONCLUSIONS

This paper presented a dynamic analysis of MMC-based MTDC grids, focused on the study of different control approaches of the management of the MMC internally stored energy. By using detailed MMC models suitable for small-signal stability analysis, the methodology for obtaining linearized MTDC models was presented. The linear models are validated with time-domain simulations in comparison to a detailed EMT model. With the Singular Value Decomposition method, the obtained models are exploited to identify the impact of MMC *Energy-based* controllers on the DC voltage behavior and arm capacitor voltages. For a given DC voltage limitation range in steady-state and during transients, it is shown that the proportional droop control technique is inefficient for limiting the DC voltage variations for the whole frequency range without further MMC control modifications. In small MTDC grids, it may possibly be allowed to loosen the imposed limitation, but with targeted improvements on the MMC control (without changing the droop value), the DC voltage deviations can be reduced even for fast dynamics. In this paper, it is proven that the DC voltage deviations can be effectively limited if each MMC can use its own dedicated internal energy management control strategy for increasing the effective DC capacitance of the whole DC grid (even the MMCs connected to wind farms without droop controller). This feature is particularly interesting in HVDC projects where the premature aging of the cable and accessories is one of the main concerns. Furthermore, two different options were studied in this paper, but it is expected that new strategies will arise based on the MMC energy management approach.

APPENDIX

A. System Parameters

The cable and MMC parameters are listed in Tables III and IV, respectively. The variables $\tau_{\text{"x"}}$ and $\zeta_{\text{"x"}}$ are the response times and damping coefficients for the controller of "x".

B. MMC-SSTI non-linear model equations

The expressions for the modulated voltages $\boldsymbol{v^{\Delta}_{mdq}}$ and $\boldsymbol{v^{\Sigma}_{mdqz}}$ are shown in (25) (at the bottom of the page). In (26), (27) and (28), the dynamic equations for $\boldsymbol{i^{\Sigma}_{dqz}}$, $\boldsymbol{v^{\Sigma}_{Cdqz}}$ and $\boldsymbol{v^{\Delta}_{CdqZ}}$ are respectively shown.

$$\frac{d\boldsymbol{i^{\Sigma}_{dqz}}}{dt} = \begin{bmatrix} 0 \\ 0 \\ \frac{v_{dc}}{2L_{arm}} \end{bmatrix} - \frac{\boldsymbol{v^{\Sigma}_{mdqz}}}{L_{arm}} - \frac{R_{arm}}{L_{arm}}\boldsymbol{i^{\Sigma}_{dqz}} + \begin{bmatrix} +2\omega i_q^{\Sigma} \\ -2\omega i_d^{\Sigma} \\ 0 \end{bmatrix} \tag{26}$$

$$\frac{d\boldsymbol{v^{\Sigma}_{Cdqz}}}{dt} = \begin{bmatrix} 2\omega v_{Cq}^{\Sigma} & -2\omega v_{Cd}^{\Sigma} & 0 \end{bmatrix}^{\top} + \frac{1}{8C_{arm}} \begin{bmatrix} 4i_z^{\Sigma} & 0 & 4i_d^{\Sigma} & i_d^{\Delta} & -i_q^{\Delta} \\ 0 & 4i_z^{\Sigma} & 4i_q^{\Sigma} & -i_q^{\Delta} & -i_d^{\Delta} \\ 2i_d^{\Sigma} & 2i_q^{\Sigma} & 4i_z^{\Sigma} & i_d^{\Delta} & i_q^{\Delta} \end{bmatrix} \begin{bmatrix} \boldsymbol{m^{\Sigma}_{dqz}} \\ \hline \boldsymbol{m^{\Delta}_{dq}} \end{bmatrix} \tag{27}$$

$$\frac{d\boldsymbol{v^{\Delta}_{CdqZ}}}{dt} = \begin{bmatrix} -\omega v_{Cq}^{\Delta} & \omega v_{Cd}^{\Delta} & -3\omega v_{CZ_q}^{\Delta} & 3\omega v_{CZ_d}^{\Delta} \end{bmatrix}^{\top} + \frac{1}{8C_{arm}} \begin{bmatrix} i_d^{\Delta} & -i_q^{\Delta} & 2i_d^{\Delta} & 2i_d^{\Sigma} + 4i_z^{\Sigma} & -2i_q^{\Sigma} \\ -i_q^{\Delta} & -i_d^{\Delta} & 2i_q^{\Delta} & -2i_q^{\Sigma} & 4i_z^{\Sigma} - 2i_d^{\Sigma} \\ i_d^{\Delta} & i_q^{\Delta} & 0 & 2i_d^{\Sigma} & 2i_q^{\Sigma} \\ i_q^{\Delta} & -i_d^{\Delta} & 0 & -2i_q^{\Sigma} & 2i_d^{\Sigma} \end{bmatrix} \begin{bmatrix} \boldsymbol{m^{\Sigma}_{dqz}} \\ \hline \boldsymbol{m^{\Delta}_{dq}} \end{bmatrix} \tag{28}$$

The Park transformation adopted in this paper is shown in (29), where n takes the value 1 or -2 for "Δ" or "Σ" variables, respectively.

$$\boldsymbol{P}_{n\omega} = \frac{2}{3} \begin{bmatrix} \cos(n\omega t) & \cos(n\omega t - \frac{2\pi}{3}) & \cos(n\omega t - \frac{4\pi}{3}) \\ \sin(n\omega t) & \sin(n\omega t - \frac{2\pi}{3}) & \sin(n\omega t - \frac{4\pi}{3}) \\ \frac{1}{2} & \frac{1}{2} & \frac{1}{2} \end{bmatrix} \tag{29}$$

C. MMC Total energy calculation

The energy stored in the upper and lower arms, respectively W_j^U and W_j^L with $j \in [a, b, c]$, are calculated as follows:

$$W_j^U = \frac{1}{2}C_{arm}\left(v_{Cj}^U\right)^2; \quad W_j^L = \frac{1}{2}C_{arm}\left(v_{Cj}^L\right)^2 \tag{30}$$

The total energy W_z^{Σ} is defined in this paper as:

$$W_z^{\Sigma} = W_a^U + W_a^L + W_b^U + W_b^L + W_c^U + W_c^L \tag{31}$$

$$\begin{bmatrix} \boldsymbol{v^{\Sigma}_{mdqz}} \\ \hline \boldsymbol{v^{\Delta}_{mdq}} \end{bmatrix} = \frac{1}{4} \left[\begin{array}{ccccc} 2v_{Cz}^{\Sigma} & 0 & 2v_{Cd}^{\Sigma} & v_{Cd}^{\Delta} + v_{CZ_d}^{\Delta} & v_{CZ_q}^{\Delta} - v_{Cq}^{\Delta} \\ 0 & 2v_{Cz}^{\Sigma} & 2v_{Cq}^{\Sigma} & -v_{Cq}^{\Delta} - v_{CZ_q}^{\Delta} & v_{CZ_d}^{\Delta} - v_{Cd}^{\Delta} \\ v_{Cd}^{\Sigma} & v_{Cq}^{\Sigma} & 2v_{Cz}^{\Sigma} & v_{Cd}^{\Delta} & v_{Cq}^{\Delta} \\ \hline -v_{Cd}^{\Delta} - v_{CZ_d}^{\Delta} & v_{Cq}^{\Delta} + v_{CZ_q}^{\Delta} & -2v_{Cd}^{\Delta} & -v_{Cd}^{\Sigma} - 2v_{Cz}^{\Sigma} & v_{Cq}^{\Sigma} \\ v_{Cq}^{\Delta} - v_{CZ_q}^{\Delta} & v_{Cd}^{\Delta} - v_{CZ_d}^{\Delta} & -2v_{Cq}^{\Delta} & v_{Cq}^{\Sigma} & v_{Cd}^{\Sigma} - 2v_{Cz}^{\Sigma} \end{array}\right] \begin{bmatrix} \boldsymbol{m^{\Sigma}_{dqz}} \\ \hline \boldsymbol{m^{\Delta}_{dq}} \end{bmatrix} \tag{25}$$

REFERENCES

[1] A. Lesnicar and R. Marquardt, "An innovative modular multilevel converter topology suitable for a wide power range," in *IEEE Power Tech Conference*, vol. 3, pp. 6 pp. Vol.3–, June 2003.

[2] L. Zhao, H. Rao, X. Li, W. Zhang, Y. Xiang, and M. Fu, "Development of ±160 kV XLPE cable and its application to the world's first three-terminal VSC HVDC system in China," in *AORC-CIGRE*, 2014.

[3] E. Prieto-Araujo, A. Egea-Alvarez, S. Fekriasl, and O. Gomis-Bellmunt, "DC voltage droop control design for multiterminal HVDC systems considering AC and DC grid dynamics," *IEEE Trans. on Power Del.*, vol. 31, pp. 575–585, April 2016.

[4] P. Rault, X. Guillaud, F. Colas, and S. Nguefeu, "Investigation on interactions between AC and DC grids," in *IEEE Grenoble PowerTech*, pp. 1–6, June 2013.

[5] W. Wang, M. Barnes, and O. Marjanovic, "Frequency-response analysis and compensator enhancement of droop control for VSC-HVDC," in *11th IET International Conference on AC and DC Power Transmission*, pp. 1–8, Feb 2015.

[6] G. Stamatiou and M. Bongiorno, "Power-dependent droop-based control strategy for multi-terminal HVDC transmission grids," *IET Gen., Trans. & Distr.*, vol. 11, no. 2, pp. 383–391, 2017.

[7] Y. Li, G. Tang, J. Ge, Z. He, H. Pang, J. Yang, and Y. Wu, "Modeling and damping control of modular multilevel converter based DC grid," *IEEE Trans. on Power Systems*, vol. 33, no. 1, pp. 723–735, 2018.

[8] X. Lu, W. Xiang, W. Lin, and J. Wen, "Small-signal modeling of MMC based DC grid and analysis of the impact of DC reactors on the small-signal stability," *International Journal of Electrical Power & Energy Systems*, vol. 101, pp. 25 – 37, 2018.

[9] A. E. Leon, "Short-term frequency regulation and inertia emulation using an MMC-based MTDC system," *IEEE Trans. on Power Systems*, vol. 33, pp. 2854–2863, May 2018.

[10] R. H. Renner and D. V. Hertem, "Potential of wind farms connected to HVDC grid to provide DC ancillary services," *IEEE Trans. on Sustainable Energy*, vol. 9, pp. 1011–1020, July 2018.

[11] W. Yang, Q. Song, and W. Liu, "Decoupled control of modular multilevel converter based on intermediate controllable voltages," *IEEE Trans. Ind. Electron.*, vol. 63, pp. 4695–4706, Aug 2016.

[12] J. Freytes, P. Rault, F. Gruson, F. Colas, and X. Guillaud, "Dynamic impact of MMC controllers on DC voltage droop controlled MTDC grids," in *18th European Conference on Power Electronics and Applications*, pp. 1–10, Sept 2016.

[13] E. Sánchez-Sánchez, E. Prieto-Araujo, A. Junyent-Ferré, and O. Gomis-Bellmunt, "Analysis of MMC energy-based control structures for VSC-HVDC links," *IEEE Trans. Emerg. Sel. Topics Power Electron.*, vol. 6, pp. 1065–1076, Sept 2018.

[14] K. Shinoda, A. Benchaib, J. Dai, and X. Guillaud, "Virtual capacitor control: Mitigation of DC voltage fluctuations in MMC-based HVDC systems," *IEEE Trans. on Power Del.*, vol. 33, no. 1, pp. 455–465, 2018.

[15] T. Li, A. M. Gole, and C. Zhao, "Harmonic instability in MMC-HVDC converters resulting from internal dynamics," *IEEE Trans. on Power Del.*, vol. 31, no. 4, pp. 1738–1747, 2016.

[16] A. Jamshidifar and D. Jovcic, "Small-signal dynamic DQ model of modular multilevel converter for system studies," *IEEE Trans. on Power Del.*, vol. 31, pp. 191–199, Feb 2016.

[17] G. Bergna-Diaz, J. Freytes, X. Guillaud, S. D'Arco, and J. A. Suul, "Generalized Voltage-based State-Space Modelling of MMC with Constant Equilibrium in Steady-State," *IEEE Trans. Emerg. Sel. Topics Power Electron.*, vol. 6, pp. 707–725, June 2018.

[18] J. Freytes, G. Bergna, J. A. Suul, S. D'Arco, F. Gruson, F. Colas, H. Saad, and X. Guillaud, "Improving small-signal stability of an MMC with CCSC by control of the internally stored energy," *IEEE Trans. on Power Del.*, vol. 33, no. 1, pp. 429–439, 2018.

[19] H. Saad, S. Dennetière, J. Mahseredjian, P. Delarue, X. Guillaud, J. Peralta, and S. Nguefeu, "Modular multilevel converter models for electromagnetic transients," *IEEE Trans. on Power Del.*, vol. 29, pp. 1481–1489, June 2014.

[20] G. Bergna, J. A. Suul, and S. D'Arco, "State-space modelling of modular multilevel converters for constant variables in steady-state," in *IEEE 17th Workshop on Control and Modeling for Power Electronics*, pp. 1–9, June 2016.

[21] J. Freytes, G. Bergna, J. A. Suul, S. D'Arco, H. Saad, and X. Guillaud, "State-space modelling with steady-state time invariant representation of energy based controllers for modular multilevel converters," in *IEEE Manchester PowerTech*, pp. 1–7, June 2017.

[22] G. Pinares and M. Bongiorno, "Modeling and analysis of VSC-based HVDC systems for DC network stability studies," *IEEE Trans. on Power Del.*, vol. 31, pp. 848–856, April 2016.

[23] N. R. Chaudhuri, R. Majumder, B. Chaudhuri, and J. Pan, "Stability analysis of VSC MTDC grids connected to multimachine AC systems," *IEEE Trans. on Power Del.*, vol. 26, pp. 2774–2784, Oct 2011.

[24] Q. Tu, Z. Xu, and L. Xu, "Reduced Switching-Frequency Modulation and Circulating Current Suppression for Modular Multilevel Converters," *IEEE Trans. on Power Del.*, vol. 26, pp. 2009–2017, July 2011.

[25] X. Wang, Y. Song, and M. Irving, "Small-Signal Stability Analysis of Power Systems," in *Modern power systems analysis*, pp. 266–290, Boston, MA, USA: Springer, 2008.

[26] J. Freytes, S. Akkari, J. Dai, F. Gruson, P. Rault, and X. Guillaud, "Small-signal state-space modeling of an HVDC link with modular multilevel converters," in *IEEE 17th Workshop on Control and Modeling for Power Electronics*, pp. 1–8, June 2016.

[27] J. Beerten, S. D'Arco, and J. A. Suul, "Frequency-dependent cable modelling for small-signal stability analysis of VSC-HVDC systems," *IET Gen., Trans. & Distr.*, vol. 10, pp. 1370–1381(11), April 2016.

[28] A. Elahidoost and E. Tedeschi, "Expansion of offshore HVDC grids: An overview of contributions, status, challenges and perspectives," in *IEEE 58th International Scientific Conference on Power and Electrical Engineering of Riga Technical University*, pp. 1–7, Oct 2017.

[29] CIGRÉ B4, "TB 684 2017 Recommended voltages for HVDC grids," tech. rep., 2017.

[30] S. Skogestad and I. Postlethwaite, *Multivariable Feedback Control: Analysis and design*. John Wiley & Sons, 2007.

[31] S. Akkari, E. Prieto-Araujo, J. Dai, O. Gomis-Bellmunt, and X. Guillaud, "Impact of the dc cable models on the SVD analysis of a multi-terminal HVDC system," in *Power Systems Computation Conference (PSCC)*, pp. 1–6, June 2016.

[32] K. Rouzbehi, J. I. Candela, G. B. Gharehpetian, L. Harnefors, A. Luna, and P. Rodriguez, "Multiterminal DC grids: Operating analogies to AC power systems," *Renewable and Sustainable Energy Reviews*, vol. 70, pp. 886 – 895, 2017.

[33] E. Prieto-Araujo, F. Bianchi, A. Junyent-Ferré, and O. Gomis-Bellmunt, "Methodology for droop control dynamic analysis of multiterminal VSC-HVDC grids for offshore wind farms," *IEEE Trans. on Power Del.*, vol. 26, pp. 2476–2485, Oct 2011.

[34] G. Bergna, J. A. Suul, and S. D'Arco, "Impact on small-signal dynamics of using circulating currents instead of AC-currents to control the DC voltage in MMC HVDC terminals," in *IEEE Energy Conversion Congress and Exposition (ECCE)*, pp. 1–8, Sept 2016.

Julian Freytes (S'15 - M'18) received the Electrical Engineering degree from the Universidad Nacional del Sur (UNS), Bahía Blanca, Argentina in 2013. He received the M.Sc. degree in Electrical Engineering for Sustainable Development from the Université des Sciences et Technologies de Lille, France in 2014. In 2017, he obtained his Ph.D. at Centrale Lille, France. He currently works at Grid Solutions, GE Power, Massy, France. His main research interests include the modeling and control of power electronics for HVDC systems.

Samy Akkari graduated from the École Normale Supérieure (ENS) of Cachan, France, in Electrical Engineering and passed his M.Sc. degree in Renewable Energy, Science and Technology from École Polytechnique ParisTech in 2013. He holds a Ph.D. on the control of Multi-Terminal HVDC systems from the engineering school of Centrale-Supélec and the university of Paris-Saclay, and currently works as an O&M Engineer for HVDC Projects at Réseau de Transport d'Électricité (RTE), France.

Pierre Rault obtained a Ph.D. degree at Ecole Centrale de Lille in 2014, entitled "Dynamic Modeling and Control of Multi-Terminal HVDC Grids". His researches were realized in collaboration with Réseau de Transport d'Electricité (RTE, French TSO). He currently works as a Senior Engineer for HVDC research and development activities at RTE, France.

Mohamed Moez Belhaouane received the master's degree in Automatic Control and the Ph.D. degree in Electrical Engineering from Ecole Supérieure des Sciences et Techniques de Tunis (ESSTT) and Polytechnic School of Tunisia (EPT) in 2005 and 2011, respectively. He is currently a senior research engineer in the Laboratoire d'Electrotechnique et d'Electronique de Puissance (L2EP) at Centrale Lille, France. Prior to join the Electric Grid Research Team at L2EP, he was an Associate Professor at Ecole Nationale Suprieure d'Ingénieurs de Tunis (ENSIT). Earlier, he was also an Assistant Professor in Ecole Nationale d'Ingénieurs de Gabès. His main research interests concern the modeling, analysis and control issues based on the integration of high voltage power electronic converters in HVDC and MTDC transmission systems. In addition, his research advances include also the implementation of advanced control strategies using HIL and PHIL concepts based on small-scale multi-terminal DC mock-up. Finally, his research and development (R&D) woks are mainly related to Réseau de Transport d'Electricité (RTE, French TSO).

François Gruson received the Ph.D. degree in electrical engineering from the Ecole Centrale de Lille, in 2010. Since 2011, he has been working as Associate Professor at Arts et Métiers ParisTech in the Laboratoire d'Electrotechnique et d'Electronique de Puissance of Lille (L2EP), Lille, France. His research interests include power electronic converter and power quality for distribution and transmission grid application and especially for HVDC transmission.

Frédéric Colas was born in Lille, France, on October 17, 1980. He received a Ph.D. in control system in 2007 from Ecole Centrale de Lille, France. Frédéric Colas is a member of the Laboratoire d'Electrotechnique et d'Electronique de Puissance of Lille (L2EP) and is a Research Engineer at Arts et Métiers ParisTech, 8 boulevard Louis XIV, 59046 Lille, France. His field of interest includes the integration of dispersed generation systems in electrical grids, advanced control techniques for power system and hardware-in-the-loop simulation.

Xavier Guillaud (M'04) has been professor in Laboratoire d'Electrotechnique et d'Electronique de Puissance of Lille (L2EP) Centrale Lille since 2002. First, he worked on the modeling and control of power electronic systems. Then, he studied the integration of distributed generation and especially renewable energy in power systems. Nowadays, he is studying the high voltage power electronic converters in transmission system. He is leading the development of an experimental facility composed of actual power electronic converters interacting with virtual grids modeled in real-time simulator. He is involved on several projects about power electronic on the grid within European projects and different projects with French companies.